Available online at www.sciencedirect.com

SCIENCE DIRECT®

Nuclear Instruments and Methods in Physics Research A 557 (2006) 648–656

NUCLEAR INSTRUMENTS & METHODS IN PHYSICS RESEARCH Section A

www.elsevier.com/locate/nima

DEMIN: A neutron spectrometer, Micromegas-type, for inertial confinement fusion experiments

M. Houry[a,*], E. Delagnes[b], D. Riz[a], B. Canaud[a], L. Disdier[a], F. Garaude[a], Y. Giomataris[b], V.Yu. Glebov[c], Ph. Legou[b], Ph. Rebourgeard[b], C. Sangster[c]

[a]*CEA, DAM-Ile de France BP12, 91680 Bruyères-le-Châtel, France*
[b]*CEA, DSM/DAPNIA, 91191 Gif-sur-Yvette, France*
[c]*Laboratory for Laser Energetics, Rochester NY 14623-1299, USA*

Received 9 September 2005; received in revised form 3 November 2005; accepted 22 November 2005

Abstract

A new neutron diagnostic has been designed to achieve high energy neutron spectroscopy in large γ background. The concept is based on the association of a Micromegas detector with a neutron-to-charged particle converter. Studies have been performed with a neutron generator and γ-ray sources and it has been shown that 14 MeV neutrons can be detected with improved efficiency and relative γ insensitivity. This low γ sensitivity makes this concept appealing for inertial fusion experiments. Experiments have been performed on the 60 beams, 30 kJ OMEGA laser system at the University of Rochester and have demonstrated the applications of this detector.

PACS: 52.57−z; 29.30.Hs; 29.40.Cs

Keywords: ICF diagnostic; Neutron spectrum; Micromegas; Gaseous detector

---

1. Introduction

Laser MégaJoule facility (LMJ) in France [1] and National Ignition Facility (NIF) in the USA [2] plan to achieve the ignition of deuterium-tritium (*DT*) filled capsules by inertial confinement fusion (ICF). Laser energy will compress the capsule and initiates a thermonuclear burn wave if the fuel areal density, $\langle\rho.R\rangle$, is adequate to trap the alpha particles and to use their energy to heat the fuel. In these experiments the $\langle\rho.R\rangle$ may be measured using neutrons output from the imploded capsule, like secondary neutrons produced in *DD* capsules and downscattered and tertiary neutrons in *DT* capsules [3,4]. Measurement of these neutrons remains a challenge as the γ and scattered neutrons induced by primary neutrons interactions on the experimental hardware can blind detectors. We propose a novel diagnostic to achieve neutron spectroscopy in a high γ background. We present the main characteristics of this diagnostic, called DEMIN (DEtector MIcromegas for Neutrons) and the measurement of the γ insensitivity observed at the OMEGA Facility [5].

2. Secondary and tertiary neutrons as a $\langle\rho.R\rangle$ measurement

The thrust of this paper is to measure $\langle\rho.R\rangle$ by studying neutrons which have been produced by interaction of fusion products with the fuel. The primary neutrons are produced in both *DD* and *DT* fusion with an energy of 2.45 and 14.1 MeV:

$$D + D \rightarrow p + T^* \tag{1}$$

$$\rightarrow n_{2.45} + He^3 \tag{2}$$

$$D + T \rightarrow n_{14} + He^4. \tag{3}$$

In *DD* filled capsule, secondary neutrons (n_{sec}, ranging from 12 to 17 MeV) originate from in-flight fusion between

---

[*] Corresponding author. Tel.: +0033 0 1 69 26 5.
E-mail address: michael.houry@cea.fr (M. Houry).

0168-9002/$ - see front matter © 2005 Elsevier B.V. All rights reserved.
doi:10.1016/j.nima.2005.11.184

the T^* produced by DD fusion (reaction (1)) and a deuterium atom at rest in the fuel:

$$T^* + D \to n_{\mathrm{sec}} + He^4. \tag{4}$$

The primary to secondary neutron ratio is given by relation (11):

$$Y_{\mathrm{sec}}/Y_{2.45} = \int_{E_k}^{0} \sigma_f(E_k).\frac{N_a.\rho}{M}.\frac{\mathrm{d}x}{\mathrm{d}E}.\mathrm{d}E \tag{5}$$

where $\sigma_f(E_k)$ is the cross-section of the DT^* fusion at the triton energy E_k, N_a is the Avogadro number, M is the mass of the fuel in a.u. and $\mathrm{d}E/\mathrm{d}x$ is the stopping power of the triton in the fuel.

In DT filled capsule, a fraction of primary 14.1 MeV neutrons can suffer scattering on deuterium or tritium ions by (n, n') or $(n, 2n)$ reactions. The energy band of downscattered neutrons, (n'), is below 14.1 MeV. The high-speed deuterium and tritium can interact with atoms of the fuel. The $D + T$ reaction is the most probable in-flight fusion and leads to tertiary neutron emission (n_{ter}, ranging from 9.5 to 30 MeV). In DT filled capsule, the secondary reactions are given by reactions (6) and (7) and tertiary reaction by (8):

$$n_{14} + D(T) \to n' + D^*(T^*) \tag{6}$$

$$n_{14} + D(T) \to 2n' + p^*(D^*) \tag{7}$$

$$T^*(D^*) + D(T) \to n_{\mathrm{ter}} + He^4. \tag{8}$$

The number of tertiary neutron is given by relations (9) and (10):

$$Y_{T^*,D^*}/Y_{14} = \frac{3}{4}.\sigma_e^k.\frac{N_a}{M}.\langle \rho.R \rangle \tag{9}$$

$$Y_{\mathrm{ter}}/Y_{14} = Y_{T^*,D^*}.\int_{E_k}^{0} \sigma_f^k(E_k).\frac{N_a.\rho}{M}.\frac{\mathrm{d}x}{\mathrm{d}E}.\mathrm{d}E \tag{10}$$

where σ_e^k is the scattering cross-section of 14 MeV neutron on deuterium or tritium, σ_f^k is the DT fusion at the triton or deuteron energy E_k.

If the slowing down of the recoil ions (D^* and T^*) is negligible, ratios above are reduced using the relation

$$\langle \rho.R \rangle = \int_0^E \left(\frac{\mathrm{d}E}{\rho.\mathrm{d}x}\right)^{-1}.\mathrm{d}E. \tag{11}$$

Then, secondary and tertiary neutrons to primary neutron ratios are proportional to $\langle \rho.R \rangle$ and $\langle \rho.R \rangle^2$, respectively, for DD and DT target. However, for an ignition capsule, the range of the recoil deuteron and triton is less than the radius R of the capsule. It has been shown that the slowing down of high-speed deuterium and tritium is sensitive to the electron temperature and $\langle \rho.R \rangle$ [6]. Hence, yields and spectra of these neutrons will provide a measure of the slowing down of recoil ions and then a determination of $\langle \rho.R \rangle$ [7,8]. The fraction of downscattered neutrons is also an increasing function of $\langle \rho.R \rangle$, and in the limit of small $\langle \rho.R \rangle$ is proportional to $\langle \rho.R \rangle$ [9].

From an experimental point of view, a number of other processes can create neutrons which might interfere with the measurement of secondary, downscattered and tertiary neutrons. In the case of DD capsule, contribution of other processes is not significant in the energy window of secondary neutrons. Moreover, due to their well separated energy, secondary and primary neutrons can be discriminated by time-of-flight measurement. For DT capsule, the tertiary neutron measurement is more complicate since there is overlaps with primary neutrons and neutrons from other reactions which may not be directly related to the $\langle \rho.R \rangle$. Ignition experiments on LMJ and NIF are scheduled after 2010, also simulations are helpful to design the future diagnostics. Simulations have been performed to calculate the contribution of neutrons coming from processes other than the reactions (6), (7) and (8) in the energy window of downscattered and tertiary neutrons. To achieve this analysis, we first used a hydrocode that steps through the evolution of the imploding target, and then we ran the Diane post-processor to follow the ions and the neutrons transport at each time step. Diane is a Monte Carlo code which solves the Boltzmann–Fokker–Planck equation for the charged particle in flight and the Boltzmann equation for the neutrons [10]. Fig. 1 shows calculated neutron spectra emitted from a cryogenic DT high-gain direct-drive target-design for LMJ [11,12]. The total spectrum is reported on both plots. In these plots, all the processes are taken into account. The left part of the figure shows the spectrum of direct tertiary neutron output coming from chain reactions (6) then (8) or (7) then (8), and the ratio of these tertiary neutrons to the total spectrum. The right part of the figure shows the spectrum of downscattered neutrons (reactions (6) and (7)) and their fraction. These calculations show that reactions (6)–(8) are the main production channels of neutrons above 20 MeV (more than 70%). Additional calculations have shown that the other neutrons comemainly from the following sequence: the primary 14 MeV neutrons do at least two scattering with ions, these scattered neutrons create high speed D and T, and these in turn produce tertiary neutrons by in-flight fusion. These neutrons do not represent a very high perturbation for the $\langle \rho.R \rangle$ determination, and will even be lower for a less dense target. Below 20 MeV, primary neutrons and scattered primary neutrons are the main contribution of the total spectrum. The downscattered spectrum is more perturbed. The fraction of downscattered is between 70% and 80% in the restricted energy window of 9 to 12 MeV.

3. Detector description

The DEMIN is made of a neutron-to-charged particle (*ncp*) conversion foil set in front of a Micromegas detector (MICRO MEsh GAseous Structure) [13–15]. The interaction of fast neutron in the *ncp* converter produces charged particle which may be detected by the Micromegas detector. The Micromegas is a gaseous detector composed of two gas filled gaps defined by three planar electrodes. The recoil charged particle enters the Micromegas and

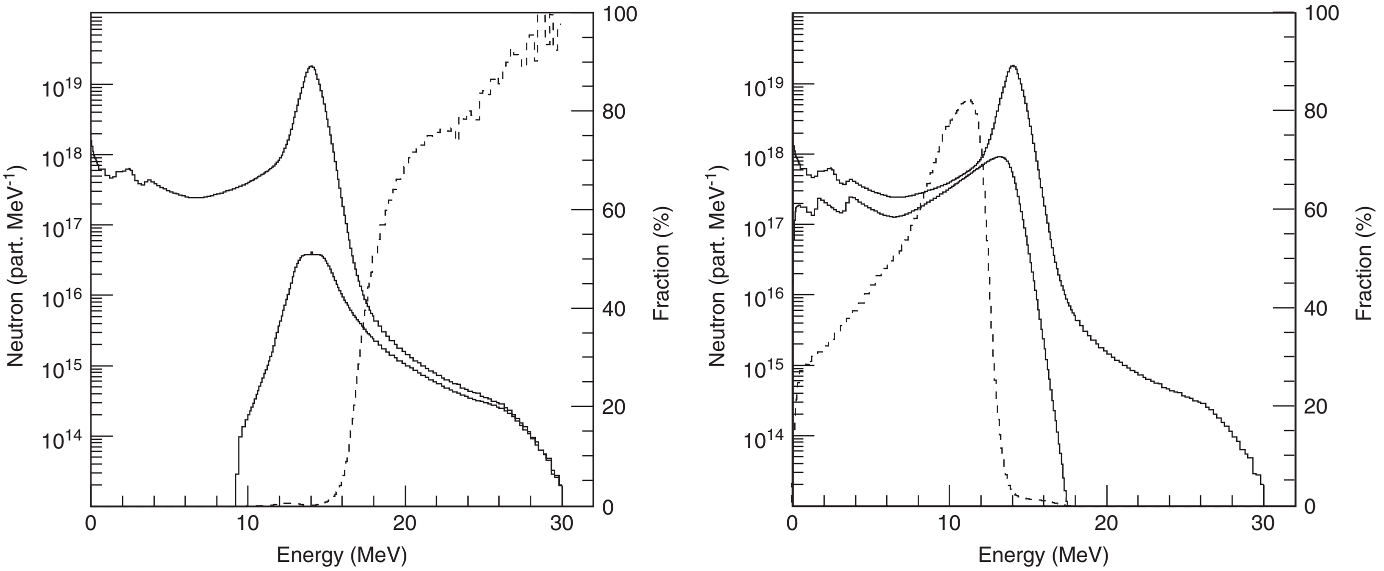

Fig. 1. Simulated neutron spectra emitted from a cryogenic *DT* high-gain direct-drive target design for the LMJ. Simulations show the contribution of tertiary (left) and downscattered (right) neutrons in the total escaping neutrons spectrum. In dashed lines are plotted the fraction of tertiary and downscattered along the energy range.

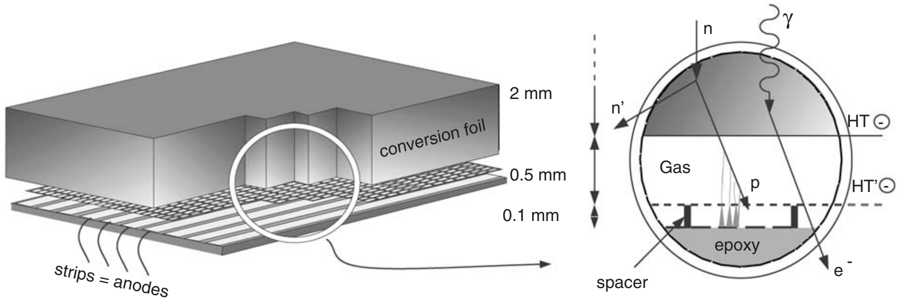

Fig. 2. Schematic view of the DEMIN diagnostic. Ionization electrons are produced along the path of scattered protons and drift between the conversion foil and the epoxy substrate. On the other hand, electrons produced by γ-rays go through the gaps with a low ionization probability.

liberates ionization electrons and positive ions in gaps. Then, as a function of polarizations applied on electrodes, the ionization electrons can drift and be multiplied by avalanche phenomena. Neutrons also interact in the gas, but considering the difference of atomic density between the *ncp* converter and the gas this second process is negligible. Fig. 2 gives a schematic view of the DEMIN concept. A negative polarization is applied on the cathode (2 μm of aluminium) stuck on the inner side of the *ncp* converter. The thickness of the aluminium foil must be weak to limit the absorption and the slowing down of the recoil charged particle. Due to the induced electric fields, electrons drift up to the strips printed on the epoxy substrate. A thin 3 μm mesh (460 pitch/inch with square holes of $50 \times 50\,\mu m^2$) separates the gap into two regions. This mesh is polarized at an intermediate voltage in order to shield the electric field created by positive ions. An $8 \times 8\,cm^2$ DEMIN detector has been designed to study the characteristics of the concept. The *ncp* conversion is made by a 2 mm thick polypropylene (CH_2). The thickness of the gaseous detector is 0.6 mm (0.5 mm thick for the upper part and 0.1 mm for the bottom part). The thickness of the gas has been chosen thin enough to limit ionization by recoil electrons: the stopping power of 1 MeV electrons is 30 eV/mm in helium, leading to a low ionization probability in 600 μm. Spacers of 150 μm diameter and 100 μm height are positioned every 1.5 mm and maintain the parallelism between the mesh and the strips. The mesh is a stainless steel cloth. Strips are 80 mm length and 1 mm width, the pitch is 1.5 mm.

After testing several gas fillings, best efficiencies are obtained with a helium–isobutane mixture. A fraction of CF_4 is added to increase the velocity of free electrons which improves the temporal shape of the signal. All presented results in the following sections have been obtained with this gas mixture.

4. Detector characteristics

A time-of-flight spectrometer must satisfy a number of requirements to perform $\langle \rho.R \rangle$ measurement. Main characteristics are the time resolution, the detection efficiency, the dynamic range but also transparency to different types of background.

4.1. Precision on the time-of-flight measurement

Secondary and tertiary neutrons are emitted during the burn time of the DT capsule on a 100 ps time scale. As the distance of neutron flight increases, neutron spectrum induces a broadening of the arrival time window: at 10 m from the capsule, the tertiary neutrons arrive in a 100 ns wide time window (37 ns for secondary neutrons). Several events may be recorded on each strip during this time window. Arrival times measured for all events on all strips give a neutron arrival time distribution and then the neutron spectrum. The resolution of the neutron spectrum will depend on the precision (Δt) of the neutron arrival time measurement. A good precision on this measurement requires a short signal with a reproducible shape and a low jitter (σ_j) on the response time to an event. Moreover, a fast signal restricts the pile-up probability, increasing the acceptable number of recorded events during the measurement time window.

The shape of the recorded signal results from two phenomena: (i) the electron collection on strips and (ii) the return current induced by ions collected on the mesh. The charge induced by electrons and ions are equal, but electrons drift faster than ions. Hence, the current pulse corresponding to electrons is tighter in time and higher. Fig. 3 shows signals recorded for one 14 MeV neutron detection in two configurations. If the electric field is low in the upper gap (−150 V; 3 kV/cm) and high in the lower gap (−450 V; 45 kV/cm), then avalanche phenomena mainly occurs between the strips and the grid. As the gas mixture is mainly helium, the signal induced by ions is going on for about 50 ns. In this configuration, the signal induced by ions is very large. This is a strong constraint for time-of-flight measurement since it increases the pile-up probability. In the second configuration, the biased voltage of the grid is set to an intermediate voltage (−180 V on the grid and −1075 V on the cathode). In order to keep high gain in electron multiplication, the biased voltage in the upper gap is increased and avalanche phenomena occur in both gaps. As shown in Fig. 3, the signal induced by ions is highly suppressed with appropriate electric fields. The fall time of the pulse is 0.8 ns and the full width at half maximum (FWHM) is 2.5 ns. In this non-conventional use of a Micromegas, the shape of signal is clearly improved and, of course, will be preferred for our time-of-flight measurements.

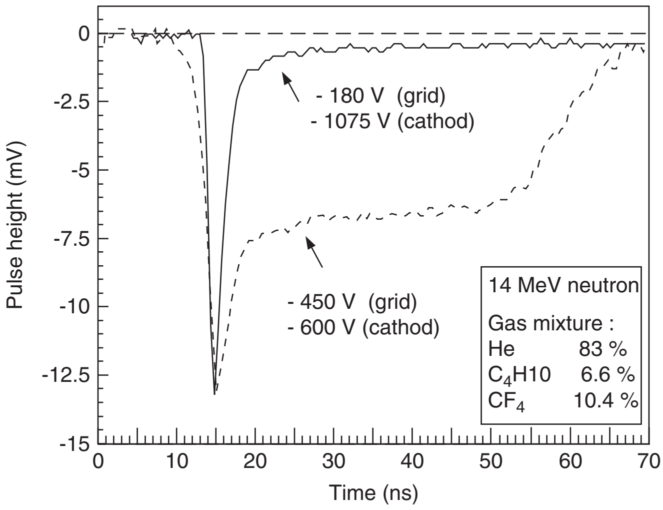

Fig. 3. Signals recorded for one 14 MeV neutron but for two electric field configurations. In dashed line, applied voltages are −450 V on the grid and −600 V on the cathode; in straight line, −180 V on the grid and −1075 V on the cathode.

The jitter on the time response to a neutron interaction is mainly due to the geometry of the detector. Charge collection occurs anywhere on the 8 cm length of the strip but signal is recorded only at one extremity of the strip. Hence, the jitter is induced by different paths of charges on the strip. The jitter σ_τ has been measured in laboratory with a picosecond's pulsed γ source (20 ps FWHM) on ELSA Facility [16]. The spectrum of γ-rays is in the range of 100 keV to 15 MeV, induced by the interaction of a pulsed 15 MeV electron beam. These experiments have shown that the jitter of the DEMIN (σ_τ) is less than 290 ps rms. This jitter, associated to the low jitter due to the acquisition system (Table 1), leads to an expected precision on the time of flight (Δt) close 300 ps rms.

The energy resolution can be then calculated with the formula

$$\frac{\Delta E}{E} \simeq \frac{\Delta t}{d} \cdot \sqrt{\frac{8.c^2.E}{M_n}} \tag{12}$$

where d is the distance from the capsule; M_n, the mass of the neutron; c, the light velocity and E, the energy of the neutron. As an example, the expected energy resolution $\Delta E/E$ is 0.3% at 10 m for 14 MeV neutrons.

4.2. Detection efficiency

For a specific neutron yield emitted in 4π, the number of recorded events will depend on the detection efficiency and the distance from the capsule. Eq. (12) shows that the energy resolution is improved with increasing the distance. Moreover, a farther location increases the measurement time window duration and then the number of recorded events by strip. This suggests to get a high detection efficiency in order to locate the detector as far away as possible from the target.

The detection efficiency is a combination of the conversion efficiency and the detection efficiency of the recoil charged particle in the gas. The conversion efficiency is the probability to get one recoil charged particle entering the gas for one incident neutron. At same cross-section reaction, this probability will decrease as the number of mass of the recoil particle increases: heaviest recoil particles are less energetic and their ranges are shorter. Hence, we use a thin hydrogenated plastic foil as an *ncp* converter. The energy of the recoil proton can be as high as 14 MeV with a range of 2.3 mm in polypropylene (0.92 g/cm^3). The elastic scattering yield with 14 MeV neutrons is about 5×10^{-3} in 2 mm of polypropylene ($\sigma = 0.76$ barn) and the transmission rate of recoil protons is about 39% [17]. This leads to a conversion efficiency of 2×10^{-3}. Entering the gaseous chamber, recoil protons liberate ionization electrons which can be amplified under the high electric field effect in the two gaps. If the charge multiplication is high enough, collected charges on strips give a signal-to-background ratio (S/B) greater than 1. Hence, assuming that all recoil protons give a signal (with $S/B > 1$), the upper limit of the detection efficiency of 14 MeV neutrons is 2×10^{-3}. Neutron can also interact with atoms of the gas, but the low density of the gas leads to a negligible detection efficiency, estimated to be lower than 10^{-6} in 600 μm of gas.

Fig. 4 presents absolute efficiency curves for 14 MeV neutrons as a function of the biased voltages applied on the grid and the cathode. The absolute efficiency is obtained by counting events with a signal over noise ratio greater than 2. The neutron source is a calibrated neutron generator. Three regions are clearly identified on the "grid–cathode biased voltage" axis: (i) Below 0 V, electric field in the upper gap is reversed and then electrons produced in this gap are not collected. The signal comes from electrons produced between the grid and the strips. Hence, biased voltage applied on the grid must be high enough to produce large electron multiplication. (ii) Between 0 and 400 V, electrons drift in the upper gap and are focussed into the multiplication gap through the grid. Whereas a large ion tail degrades the temporal shape of the signals (see Fig. 3). (iii) Electric fields are high enough to observe charge avalanche phenomena in both gaps. The efficiency increases quickly as well as for low biased voltage in the grid–anode gap. In this third mode, the gaseous detector works as a Frisch chamber, signals are faster and the ion tail is suppressed.

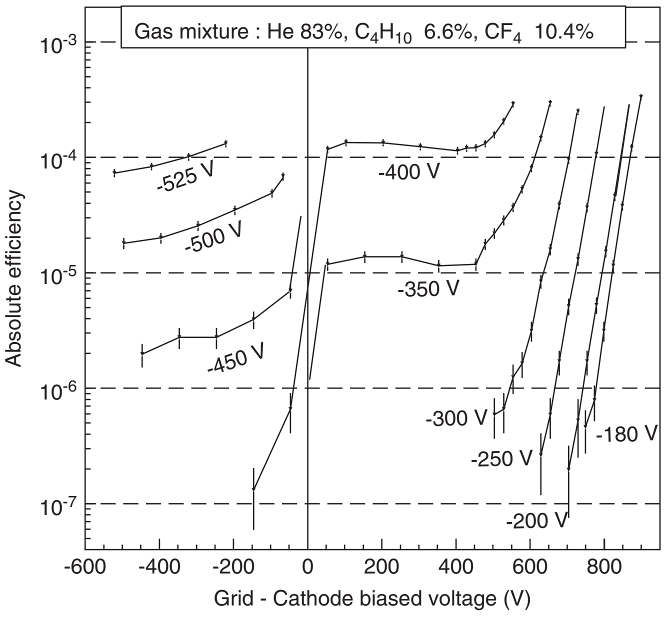

Fig. 4. Absolute efficiency curves versus the biased voltage on the grid (values are printed on curves) and the biased voltage difference between the grid and the anode (abscissa) for 14 MeV neutrons.

For these three regions, the efficiency is not measured above 4×10^{-4} because the charge multiplication becomes too important. Some events induce a strong current leading to a trip of the grid polarization or sparks.

Efficiency studies have been also performed with γ-ray sources. The interaction between γ-rays and plastic foil leads to electron emission by photoelectric effect, Compton effect or pair creation. Electrons enter the gas and create ionization electrons. The absolute efficiency curve shows a similar behaviour as the one obtained with neutrons but shifted to lower efficiencies (Fig. 4). Since the gas ionization depends on the charged particle mass, a proton or heavier charged particle creates more electron–ion pair than an electron: in 0.5 mm of helium at 1 bar, 1 MeV proton provides about 100 electron–ion pairs, whereas 1 MeV electron is below the ionization threshold. Fig. 5 compares the detection efficiency of 661 keV γ-ray and 14 MeV neutrons. The 14 MeV neutron to γ-ray efficiency ratio is better than 500 and the maximum pulse height ratio is about 10 in favour of neutrons when biased voltages are set in a neutron detection configuration. Similar measurements have been performed with other γ-ray energy (^{60}Co : 1.1 and 1.3 MeV, and ^{241}Am : 60 keV) showing similar results. These measurements show that the DEMIN diagnostic offers a relative insensitivity to γ-rays.

4.3. Dynamic range

The dynamic range is an important characteristic since the primary neutron yield can vary from 10^{14} (nowadays on OMEGA Facility) to 10^{19} (future experiments on LMJ and NIF). It will be convenient to use the diagnostic at the same location for neutron yields over several decades. Two parameters can be adjusted to modify the detection efficiency: the type of the converter and electric fields in the gaps.

In the lower limit without converter, the neutron-to-charged particle conversion occurs in the gas. In this case, the calculated conversion efficiency is close 10^{-6} in helium gas. On the other hand, the best conversion efficiency, 2×10^{-3}, is obtained with a polypropylene foil 2.3 mm thick with a thin cathode (2 μm of aluminium). Depending

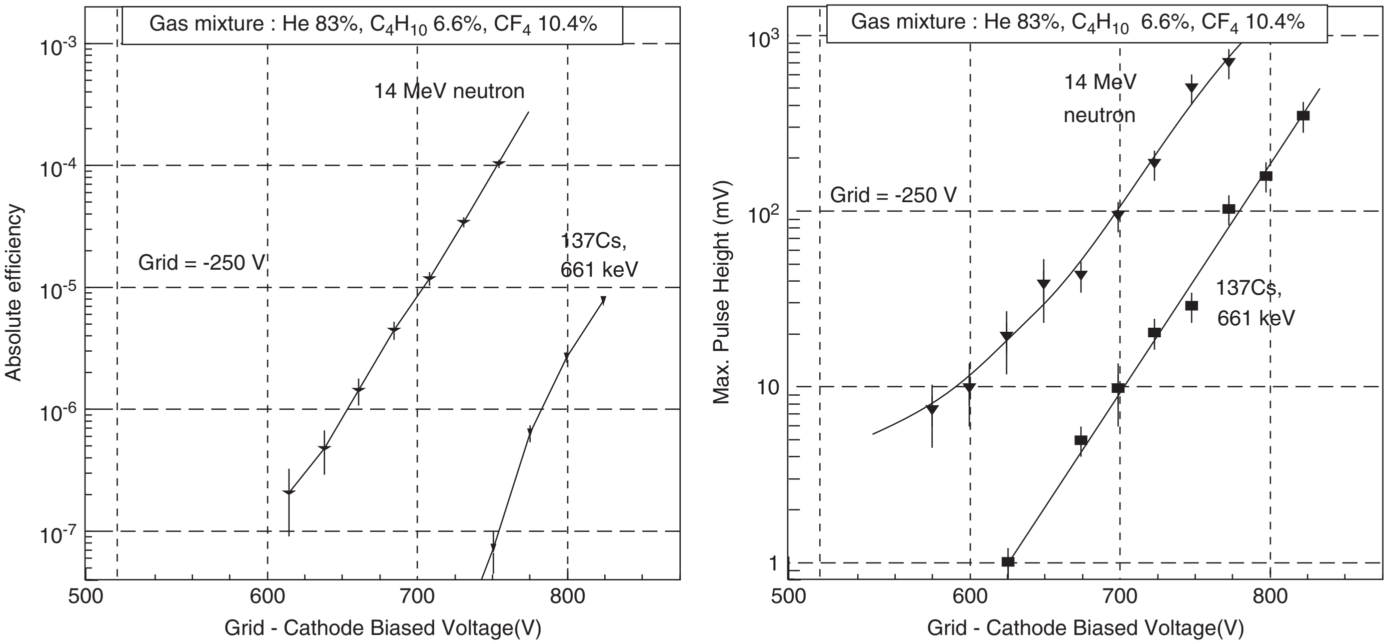

Fig. 5. Comparisons between 14 MeV neutron and 661 keV γ-rays. Plots show absolute efficiency curves (left part) and maximal pulse height (right part) as a function of the grid–cathode biased voltage. Signals are amplified by a factor of 20 (using Minicircuits preamplifiers ZFL500).

on the converter, the dynamic range of the detection efficiency covers three decades.

Moreover, the relation between the efficiency and electric fields in gaps leads to a dynamic range. Biased voltages can be adjusted in order to optimize the number of recorded events over two decades without degrading the pulse shape (Fig. 5).

As a function of the converter and electric fields, the detection efficiency is modular over five decades for a same detector location.

5. Electronic development

The data acquisition system for the DEMIN spectrometer is a digitization system. It allows more flexibility for online or offline treatments and is particularly useful in the prototyping or early phases of the experiments. The MATACQ digitization boards first developed for the DEMIN require small space and can be installed close to the detector.

5.1. *MATACQ board overview*

The MATACQ board, based on the custom MATACQ IC, is suited for acquisition of fast analog signals. It performs the coding of 4 or 8 (depending on the version) analog channels of bandwidth up to 300 MHz over a 12 bits range and at a sampling frequency reaching up to 2 GHz and over a depth of 2520 usable points. The board, in the mechanical format VME 6U (9U for the 8 channel version), is compatible with several standards of acquisition (VME, GPIB) [18].

The acquisition is realized in three steps:

- Acquisition: the analog signal is continuously sampled at the sampling frequency in the MATACQ circular analog memory. The arrival of the trigger signal initiates the stopping phase of the sampling. At the end of this phase, the state of the memory is set and contains the last 2560 points sampled (of which 2500 are valid).
- Digitization and storage: after a stopping order of the acquisition, the samples stored under analog form in the MATACQ chips are re-read (in 650 μs) and coded into digital data over 12 bits, then stored in a digital memory buffer. The acquisition is informed of the end of the coding phase either by scanning of an internal register or by an interruption.
- Reading: the memory buffer can then be re-read by the acquisition system. For an acquisition system of VME standard, the latter operation lasts a few ms for the full readout of a four-channel board, permitting the acquisition of 2500 points per channel at a frequency of few hundred Hz.

5.2. *MATACQ board triggering*

Two main modes of triggering are available on the MATACQ Board. It can be triggered either by any channel of one board crossing programmable threshold or by an external trigger input compatible with ECL or NIM standard. Thus, several MATACQ boards can be synchronized by using a common external trigger. The position of the 2500 point acquisition window relatively to the trigger is programmable on a 650 μs range. An on-chip interpolation system determines the trigger timing with a 50 ps rms precision, better than the sampling period making this board usable in a multichannel accurate timing system.

The main performances of the board are summarized in Table 1.

6. γ-ray insensitivity measurement on OMEGA Facility

Fusion neutron measurements with the DEMIN have been performed on OMEGA laser facility, University of Rochester, USA, using directly driven implosions of *DT* and *DD* fueled capsules. The capsule is located at the 320 cm-diameter target chamber centre and is imploded by 60 laser beams with an energy up to 30 kJ [19].

Table 1
Main performances and characteristics of the MATACQ board

NAME	Quantity	Unit
Input impedance	50	Ohm
Dynamic range	+/ − 0.5	V
Digitization LSB	250	μV
Noise	<200	μV rms
Analog bandwidth	300	MHz
Harmonic distortion (for 25 MHz sinus input)	< − 60	dB
Integral non-linearity	<0.5	per mil
Differential non-linearity	<0.5	per mil
Sampling frequency	1 or 2	Gsample/s
Sampling jitter	<20	ps rms
Trigger jitter	50	ps rms

6.1. *Measurements with a* scintillator + photomultiplier *(pm)*

The burn of the *DT* and *DD* targets produces high 14 and 2.45 MeV neutron yield, respectively. However, a part of these primary neutrons interact with material surrounding the target (reaction chamber, supports, grounds, walls,…) leadings to γ-rays, neutrons and charged particle emissions. The γ background and the neutron emissions have been measured at OMEGA using a calibrated detector made of a plastic scintillator and a fast photomultiplier tube. The detector was located about 8.3 m from the imploded capsule and output signals were recorded as a function of time by a TDS684 scope (Tektronics).

Figs. 6a and c show measurements performed with the scintillator + pm. In case of *DT* implosion (Fig. 6a), the signal corresponding to 14 MeV neutron detection is observed at 156 ns after the implosion of the capsule and reaches −4.8 V for 4×10^{13} neutrons emitted in 4π. Before this signal, γ-rays from neutron interactions are measured. First, we observe a small signal ($\simeq -0.7$ V at 30 ns) and a

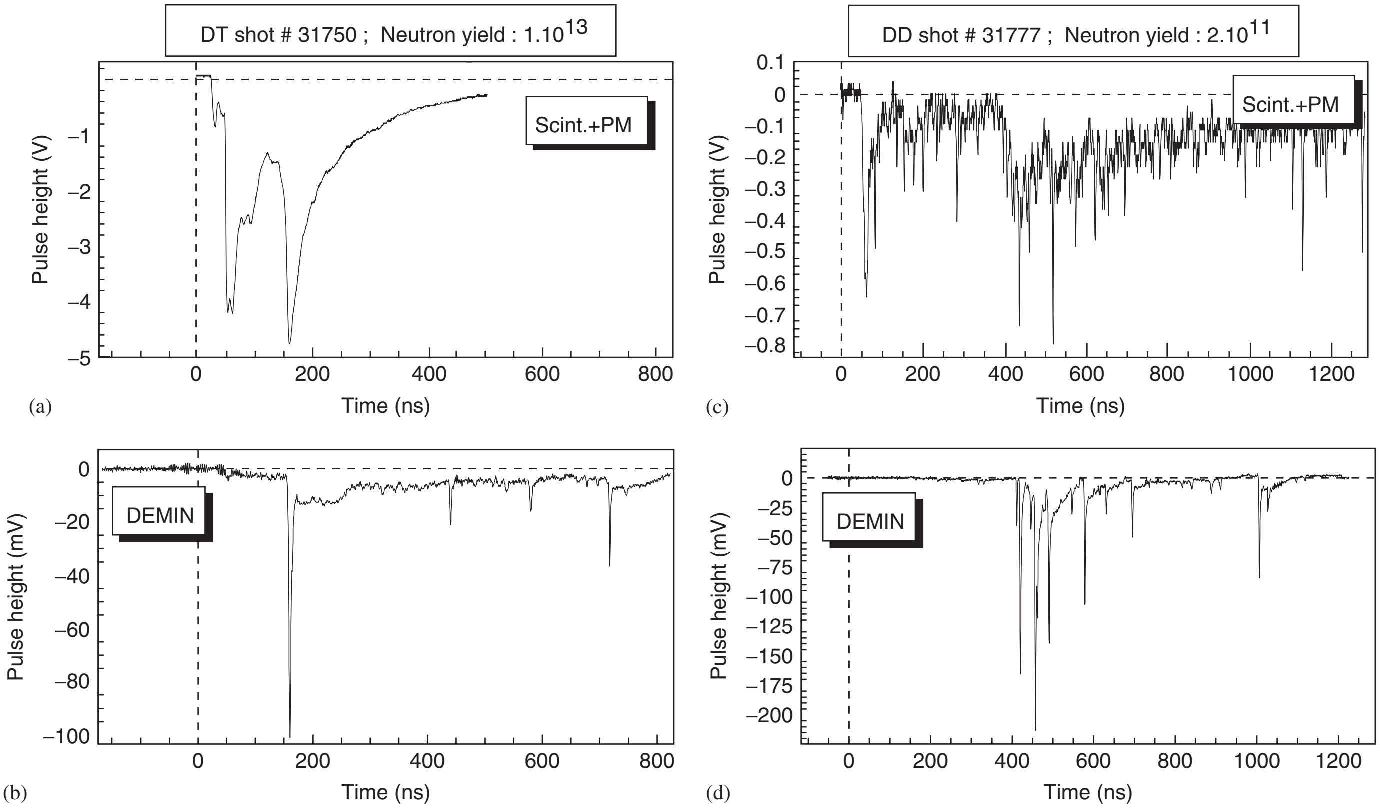

Fig. 6. Comparison of signals recorded by a scintillator + photomultiplier (pm) and by the DEMIN (using amplifiers with gain = 20) for both *DT* and *DD* target implosions. Signal from (a) scintillator + pm during *DT* shot; (b) one strip of the DEMIN during *DT* shot; (c) scintillator + pm during *DD* shot; (d) one strip of DEMIN during *DD* shot.

bigger one (−4.2 V at 55 ns) corresponding to neutron interaction with inserted mechanisms inside the chamber and with the chamber skin (made of 9 cm of aluminium), respectively. Interaction with the chamber skin is the main origin of the γ-ray background. Signal induced by γ-rays persists during several hundreds of nanoseconds. The recorded signal after the 14 MeV pulse includes both contributions of γ-rays and delayed scattered neutrons.

In case of *DD* implosion, observations are similar: γ-rays are observed before the arrival time of 2.45 MeV neutrons (Fig. 6c). However, recorded signals are weaker because yield and energy of primary neutrons are lower.

This scintillator + pm has been calibrated under high photon yields in order to estimate the γ-ray dose induced by *DT* and *DD* implosions. Simulations with TRIPOLI [20] show that the γ-ray background spectrum induced by 14 MeV neutrons in an experimental area of a laser facility and at 8.3 m from the target is very similar to the one produced by Bremstralhung of 13.6 MeV electrons in a tantale target 2 mm thick [5]. The ELSA Facility at Bruyères-le-Châtel has been used in this configuration to produce high yield of photons. Hence, the signal induced by γ-ray in the scintillator + pm (Fig. 6a) and measured before the arrival time of 14 MeV neutrons corresponds to a dose of 3 μGy in air (for a neutron yield of 4×10^{13} and a location at 8.3 m from the target).

6.2. *γ-ray insensitivity of the DEMIN*

The particle emissions for *DD* and *DT* shots were also measured with the DEMIN. The 32-channel DEMIN was located in the experimental area at 8.3 m from the target and 1 m above the groundfloor. DEMIN was in a stainless box as a shield against effects of the electromagnetic pulse (EMP). Detector signals reached preamplifiers using 1 m double-shielded cables. After a ×20 preamplification over 1 GHz bandwidth signals were sent through 5 m long double-shielded cables to the MATACQ acquisition system located underground. The read-out of the eight four-channel MATACQ boards was achieved by GPIB-optical fibre interface.

Polarizations in both gaps have been fixed at an optimal configuration for neutron spectroscopy (−250 V on the mesh and −1000 V on the cathode) with a gas mixture of He (83%), C_4H_{10} (6.6%) and CF_4 (10.4%). For these parameters, studies in laboratory show that the absolute efficiency is close to 10^{-4} and the maximum pulse height is 400 mV (Fig. 5). For a 14 MeV neutron emission of $10^{13}/4\pi$ and DEMIN located at 8.3 m from the target, about 10^4 neutrons are detected in the detection area of the DEMIN (several hundreds by strip). Events are piled up and the DEMIN works as a current mode detector. The signal on one strip is expected to be much higher than −1 V. However, the signal reaches −100 mV as shown in Fig. 6b. We think that the high yield of recoil charged particles produced by neutrons degrades electric fields in gaps of detector. The charge multiplication process is then not completed.

In case of *DD* shot (Fig. 6d), DEMIN does not work in a current mode: observed individual peaks correspond to individual neutron. Because the DEMIN has been designed for secondary and tertiary neutrons, the detection efficiency for 2.45 MeV neutron is very low.

The most important result of this first test under high neutron yield is the observation of the low γ-ray sensitivity of the DEMIN. In both *DD* and *DT* shots, the γ-ray signal arriving before primary neutrons (in the arrival time window of the secondary and tertiary neutrons) is clearly reduced compared to signals recorded by the scintillator + pm. However, the downscattered neutron time window measurement is perturbed by neutron background. Due to this neutron background, a far away location of the DEMIN is not compatible with the measurement of downscattered neutrons. For *DD* shot, γ-rays induce a signal-over-noise ratio less than 1 (for 2×10^{11} primary neutron), and for the *DT* shot, the signal reaches −4 mV (for 10^{13} primary neutrons) (Figs. 6b and d).

7. Conclusion

We propose a new diagnostic to achieve neutron spectroscopy in a high γ-ray background on inertial confinement fusion experiments. The main advantage of the DEMIN detector is a relative insensitivity to photons due to the mass dependent ionization potential in thin gaps of the chamber.

The DEMIN has been designed for 14 MeV neutron spectroscopy. Hence, the *ncp* converter is 2.3 mm thick consistent with the range of 14 MeV recoil proton in the polypropylene. This converter is a good compromise for the measurement of secondary neutrons (12–17 MeV) but will be chosen thicker for the tertiary neutrons (20–30 MeV) and thinner for the downscattered neutrons (6–9 MeV). Adjusting electric fields in the ionization gap or changing characteristics of the converter, the detection efficiency for 14 MeV neutron is versatile over several decades and can reach a maximum of 6×10^{-4}. Biased voltages on the cathode and the grid are chosen in order to set the grid at an intermediate polarization. This non-conventional use of a Micromegas detector induces avalanche phenomena in both gaps leading to a high suppression of the ion signal.

First tests performed at OMEGA Facility show that the γ-ray background is enough suppressed to allow the measurement of secondary and tertiary neutrons for the future experiments of *DD* and *DT* fusion with high $\langle \rho.R \rangle$ on OMEGA, LMJ and NIF facilities.

Actually, a larger DEMIN diagnostic with 160 channels associated to 20 eight-channel MATACQ boards is developed in order to perform secondary neutron spectroscopy at OMEGA facility during the year 2005.

Acknowledgements

This work is supported by the Direction des Applications Militaires du Commissariat à l'Energie Atomique (CEA/DAM-Ile-de-France). The authors would like to express their gratitude to the Laboratory for Laser Energetics for providing access to the Facility and technical support. The authors would like to acknowledge the assistance of the staff of the ELSA facility at CEA/DAM-Ile-de-France in making some measurements; and support from R. De Oliveira, X. Coppolani, P. Le Bourlout and O. Maillard concerning construction of the diagnostic.

References

[1] R. Pellat, Inertial Fusion Science and Applications, 2001, p.17.
[2] C.B. Tarter, in: K.A. Tanaka, et al. (Eds.), Inertial Fusion and High-energy-density Science in the US, Elsevier, Amsterdam, 2002, pp. 9–16.
[3] M.D. Cable, S.P. Hatchett, J. Appl. Phys. 62 (6) (1987) 2233.
[4] H. Azechi, et al., Laser part, Beams 9 (1991) 119.
[5] M. Houry, et al., Proceedings of the International Conference on Advanced Diagnostics for Magnetic and Inertial Fusion, Varenna, Italy, 2001.
[6] C.K. Li, D. Petrasso, Phys. Rev. Lett. 70 (1993) 3059.
[7] F.H. Séguin, et al., Phys. Plasmas 9 (2002) 2725.
[8] S. Kurebayashi, et al., Phys. Plasmas 12 (2005).
[9] D.C. Wilson, et al., Nucl. Instr. and Meth. A 488 (2002) 400.
[10] D. Riz, M. Chiche, Simulation of energetic ions transport in a plasma by a 3D Monte Carlo method, Supercomputing in Nuclear Applications, Paris, 2003.
[11] D. Riz, et al., Nucl. Fusion, submitted for publication.
[12] B. Canaud, et al., Nucl. Fusion 44 (2004) 1118.
[13] Y. Giomataris, et al., Nucl. Instr. and Meth. A 376 (1996) 29.
[14] G. Charpak, et al., Nucl. Instr. and Meth. A 478 (2002) 26.
[15] J. Pancin, et al., Nucl. Instr. and Meth. A 524 (2004) 104.
[16] R. Dei-Cas, et al., Nucl. Instr. and Meth. A 296 (1990) 209.
[17] J.F. Ziegler, J.P. Biersack, ⟨http://www.srim.org⟩.
[18] E. Delagnes, et al., IEEE Trans. Nucl. Sci., 2005, accepted for publication.
[19] T.R. Boehly, et al., Opt. Commun. 133 (1997) 495.
[20] M. André, F. Jequier, Proceedings of the Symposium on Current Trends in International Fusion Research, Washington, US, 2001.